

Natural Language-Driven Global Mapping of Martian Landforms

Yiran Wang^{1†}, Shuoyuan Wang^{1†}, Zhaoran Wei¹, Jiannan Zhao²,
Zhonghua Yao³, Zejian Xie¹, Songxin Zhang¹, Jun Huang⁴,
Bingyi Jing⁵, Hongxin Wei^{1*}

¹School of Science, Southern University of Science and Technology, Shenzhen, China.

²China University of Geosciences, Wuhan, China.

³University of Hong Kong, Hong Kong SAR, China.

⁴Hubei Key Laboratory of Planetary Geology, China University of Geosciences, Wuhan, China.

⁵The Chinese University of Hong Kong, Shenzhen, China.

*Corresponding author. Email: weihx@sustech.edu.cn

†These authors contributed equally to this work.

Planetary surfaces are typically analyzed using high-level semantic concepts in natural language, yet vast orbital image archives remain organized at the pixel level. This mismatch limits scalable, open-ended exploration of planetary surfaces. Here we present MarScope, a planetary-scale vision-language framework enabling natural language-driven, label-free mapping of Martian landforms. MarScope aligns planetary images and text in a shared semantic space, trained on over 200,000 curated image-text pairs. This framework transforms global geomorphic mapping on Mars by replacing pre-defined classifications with flexible semantic retrieval, enabling arbitrary user queries across the entire planet in ~5 sec-

onds with F1 scores up to 0.978. Applications further show that it extends beyond morphological classification to facilitate process-oriented analysis and similarity-based geomorphological mapping at a planetary scale. MarScope establishes a new paradigm where natural language serves as a direct interface for scientific discovery over massive geospatial datasets.

Introduction

Planetary science increasingly depends on the interpretation of vast and rapidly expanding remote-sensing datasets to reconstruct surface processes and environmental evolution. Scientists analyze planetary landforms using high-level geomorphological concepts, such as aeolian (1; 2), volcanic (3; 4), fluvial (5; 6), glacial (7), and impact processes (8), expressed in natural language. In contrast, planetary image archives are organized primarily by pixels, rather than by semantic geological meaning. This mismatch between human conceptual reasoning and data organization fundamentally limits scalable, open-ended exploration of planetary surfaces.

To address this challenge, researchers have focused on generating global geomorphological maps using either manual interpretation or task-specific supervised learning approaches. Manual mapping remains the gold standard for accuracy but is inherently slow, labor-intensive, and difficult to scale beyond a limited number of landform types. Supervised learning approaches can accelerate mapping for specific morphologies, yet they require large, carefully labeled training datasets and typically generalize poorly across heterogeneous landforms. As orbital image archives continue to expand in both resolution and volume (9; 10), these limitations increasingly constrain discovery, leaving planetary science “data-rich but interpretation-limited”.

Recent advances in multimodal representation learning (11) offer a promising pathway toward overcoming these limitations. Contrastive vision language models trained on paired images and text can learn high-level semantic representations that link visual patterns with linguistic concepts, enabling zero-shot and label-free retrieval using natural language prompts. Applied to planetary data, such models have the potential to move beyond pixel-level classification toward semantic representations that capture not only morphological similarity but also relationships related to surface processes and formation mechanisms, as encoded in language. Yet this opportunity remains

largely unrealized: there is still no planetary-scale multimodal system for fast, label-free retrieval of diverse landforms, nor any framework that delivers comprehensive, quantitative, cross-comparable maps of planetary geomorphology.

Results

Near instantaneous planetary-scale retrieval of Martian landforms. Here we introduce MarScope (<http://marscope.site/>), a planetary-scale visual-language platform that enables near-instantaneous (~5 s) retrieval and global mapping of Martian landforms. Trained on more than 200,000 curated planetary image–text pairs, MarScope embeds surface imagery and language into a shared vision–language space, allowing text prompts, representative images, or their combination to serve as flexible search queries (Figure 1). This semantic framework redefines global geomorphological exploration as a label-free retrieval task, enabling the identification of common landforms by text such as name or formation process, as well as previously unmapped features through images.

At its core, MarScope uses a contrastive vision–language encoder (11) that learns high-dimensional embeddings capturing diagnostic aspects of surface morphology. By representing images and text within a joint semantic space, the platform allows researchers to search, compare, and classify Martian surface features flexibly and at scale. This shift from pixel-based imaging to structured semantic understanding enables global mapping of any feature at any time.

To accommodate diverse scientific use cases, MarScope supports three complementary query modes. Text-based queries generate global distribution maps of specified landforms or their formation process (for example, yardangs, concentric crater fills, or shallow ground ice), revealing spatial patterns that would otherwise require extensive manual work. Image-based queries retrieve morphologically similar examples without predefined labels, facilitating the discovery of rare or understudied landforms such as doublet craters. Image-text multimodal queries combine visual exemplars with textual constraints to refine results for complex or heterogeneous morphologies.

The platform operates on a global mosaic of CTX data (9; 12; 13) subdivided into overlapping tiles at two spatial resolutions: a 0.2° default mode optimized for kilometre-scale features and a 0.02° high-resolution (Hi-Res) mode targeting sub-kilometre landforms. Each tile is encoded once into the shared embedding space, stored in a similarity-search index, and collectively compresses

the CTX dataset by a factor of ~ 160 . Incoming queries—text, image, or image-text—are compared against all tiles using cosine similarity, and the highest-scoring matches are projected back onto a global map and visualized as point distributions or heatmaps to show spatial extent and density.

In addition to visualization, MarScope allows direct download of matched imagery, providing ready-to-use training samples for downstream classification and recognition tasks. This greatly lowers the barrier to dataset construction and accelerates the development of specialized AI models.

Retrieval performance evaluated against global geomorphological datasets. We evaluated MarScope’s ability to recover known geomorphological patterns by comparing its outputs with six published global catalogues representing diverse surface processes: alluvial fans (14), glacier-like forms (15), landslides (16), pitted cones (17), yardangs (18) and dark slope streak (19). The first five classes were assessed using the default search mode, whereas dark slope streaks—owing to their small spatial scale—were evaluated using the high-resolution mode. For each landform type, we tested three retrieval strategies: text queries (landform name only), image queries (six representative examples), and multimodal queries (combining text and images). Published catalogues and text-mode outputs are shown in Figure 2.

Retrieval fidelity was quantified using dynamic F1 scores as a function of the top-K retrieved tiles (Figure 2, right; computation described in Methods). No single query mode performs best across all landforms, reflecting differences in morphological distinctiveness and representation within the training corpus. Pitted cones and yardangs achieve their highest F1 scores with text queries, indicating that their diagnostic morphology is well captured by semantic labels. In contrast, alluvial fans and landslides benefit from multimodal queries, where additional visual constraints improve performance. Although image-only queries generally underperform relative to text and multimodal approaches, they still retrieve relevant matches despite relying on only six exemplars, highlighting the robustness of MarScope’s visual embedding space.

Overall, retrieval performance varies systematically with landform type, and the ability to switch flexibly among text, image, and multimodal queries is essential for optimizing results. Combined with the close spatial correspondence between MarScope outputs and published catalogues, these tests demonstrate that MarScope provides a reliable and generalizable framework for rapid global reconstruction of Martian landforms.

Global mapping of diverse Martian landforms. To enable planet-scale geomorphological analysis, MarScope was used to generate global mapping of key Martian landforms across aeolian, glacial-periglacial, volcanic, and tectonic systems, providing a unified framework for addressing broad surface-process questions (Figure 3).

The aeolian system of Mars is not a uniform global sand-transport field but shows pronounced latitudinal partitioning. At the poles, extensive sand dunes are actively reworked by the seasonal CO₂ frost cycle, driving pulsed sediment transport (20; 21). Near ~60° N and ~60° S, dust devil trails (22) form high-activity belts that record strong summertime convection. At lower latitudes (0–40°), longer-term aeolian processes dominate: transverse aeolian ridges (TARs), dated to several million years (2; 23–28), are widespread across low to mid-latitudes, whereas yardangs cluster near the equator as relics of ancient, high-energy wind erosion. Slope streaks (19; 29) and wind streaks (1; 30), concentrated in the northern hemisphere, represent active surface disturbances and reflect hemispheric asymmetry arising from topographic and dust-source contrasts.

Glacial and periglacial landforms delineate a latitudinally zoned and vertically stratified cryosphere. Pedestal craters (45°–70° N/S) record the removal of metre- to tens-of-metres-thick ice-rich mantles (31; 32). Glacier-like forms (GLFs) (33) and concentric crater fills (CCFs) (34) dominate the midlatitudes, preserving stable ice–dust mixtures near the surface. In contrast, scalloped depressions indicate shallow (< 20 m) ground-ice enrichment, particularly concentrated in northern Utopia Planitia and southern Hellas, where permafrost remains active today (35; 36).

Volcanic and tectonic landforms display strong spatial clustering and coupling. The Tharsis and Elysium provinces host the most extensive volcanic activity, characterized by fossae (37; 38), lava flows (39; 40), and lava channels (41) arranged in radial and concentric patterns around major edifices. In contrast, wrinkle ridges (42) are globally distributed, recording compressional history and thermal evolution of Mars. Pitted cones, commonly interpreted as products of magma–volatile interactions (17; 43), occur independently of major volcanic centers but are concentrated in ancient sedimentary plains such as Utopia and Isidis, reflecting localized interactions between magmatism and volatile-rich substrates (44; 45).

Together, these results demonstrate that MarScope reframes geomorphological mapping from a predefined classification task into an open-ended semantic retrieval problem, enabling coherent, cross system analysis of Martian surface processes at planetary scale.

Process-oriented mapping through semantic retrieval. In addition to retrieving landforms by name, MarScope enables mapping of geomorphological features through process-based queries, allowing landforms to be explored according to their inferred formation process mechanisms rather than predefined shapes or labels. This representation allows landforms to be explored according to their inferred formation mechanisms, rather than predefined shapes or fixed taxonomies, addressing a long-standing limitation of traditional geomorphological mapping.

This process-based mapping allows hypotheses about surface processes to be explored directly at planetary scale. As shown in Figure 4, single process-oriented queries retrieve morphologically diverse yet genetically related features: ice-related queries return multiple ice-associated and collapse landforms; stress-related queries identify coherent networks of compressional and extensional structures; and flow-related queries retrieve channels, streamlined forms, and source-collapse terrains across distinct geological settings. Such integrative retrievals make it possible to examine surface processes coherently across morphologically distinct landforms at planetary scale, enabling analyses that were previously impractical.

Mapping of rare and previously unnamed landforms through visual search. Beyond its capability for large-scale mapping, MarScope enables the mapping of previously understudied or unclassified landforms. Through image-to-image retrieval, the system searches the Martian surface by visual similarity rather than predefined labels, allowing recognition of features rarely documented in existing catalogues.

A representative example is the detection of doublet craters (Figure 5A), paired impact structures formed by the near-simultaneous collision of binary asteroids (46). Recognition of them provides insight into the population and orbital dynamics of binary impactors and the mechanics of double impacts under Martian conditions. Using verified examples as visual references, MarScope retrieves morphologically similar crater pairs across global datasets within seconds, enabling the construction of a statistically robust inventory of doublet impacts. Another example is the inverted crater (Figure 5B), where sedimentary infill became indurated and more resistant to erosion than the surrounding terrain (47). As deflation stripped away softer materials, the hardened fill remained as a raised landform. Through visual similarity search, MarScope identifies analogous structures, offering new means to study sedimentary infill, diagenesis, and erosional modification on Mars.

These examples show that visual similarity search allows planetary surfaces to be explored beyond predefined taxonomies, making it possible to identify geomorphological features that are difficult to capture with conventional, label-driven mapping.

Discussion

This work moves planetary mapping beyond predefined, morphology-centric schemes toward open-ended, language-guided mapping. By enabling natural language to serve as an interface to planetary-scale image archives, MarScope facilitates near-instantaneous generation of global geomorphological distribution maps, allowing rapid exploration of planetary surfaces. Through formation mechanisms search, MarScope enables the mapping of features based on their inferred formation processes, rather than predefined shapes or labels. Additionally, the platform supports the identification of rare, transitional, and previously understudied features, enabling the exploration of landforms that may have been overlooked in traditional mapping efforts. This formulation fosters integrative exploration of planetary surfaces without requiring explicit labels or task-specific training, opening new pathways for scientific discovery.

As a foundation model, MarScope can serve as the backbone for specialized models, fine-tuned to address specific mission goals or scientific inquiries, thereby providing a versatile infrastructure that reduces the need for extensive custom model development for each new planetary dataset. This adaptability means that MarScope can support a broad spectrum of research, from basic planetary mapping to more complex tasks, such as studying planetary habitability, resource distribution, and surface dynamics over time.

MarScope's design focuses on broad, open-ended discovery rather than highly precise detection of specific landforms, which makes it less suited for tasks requiring pixel-level accuracy. The system identifies the presence of features within image tiles but does not provide pixel-level delineation. Furthermore, its fixed tile sizes (0.2° and 0.02°) reflect a trade-off between global coverage and local detail, which may result in the underrepresentation of features that are either larger than a tile or smaller than the effective resolution. These limitations are inherent in the framework's general-purpose design, which is optimized for flexible, large-scale exploration rather than specialized feature extraction.

MarScope’s performance is shaped by the quality and diversity of its training data, including image resolution, spatial coverage, and linguistic descriptions of surface features. Ongoing efforts to expand the training corpus with higher-resolution imagery, more diverse feature descriptions, and human-in-the-loop validation are expected to enhance robustness, interpretability, and retrieval fidelity. These improvements will further solidify MarScope’s role as an exploratory interface, complementing, rather than replacing, detailed physical modeling or expert interpretation.

Although demonstrated here using Mars as a case study, MarScope’s underlying approach represents a paradigm shift in how machine intelligence can mediate access to vast geospatial archives. This paradigm enables scalable, hypothesis-driven exploration across planetary bodies and scientific domains, where mapping relies on semantic reasoning rather than rigid classification. Beyond planetary science, this approach holds promise for Earth observation and other fields, where large-scale, heterogeneous datasets require high-level conceptual navigation.

Methods

Construction of planetary vision-language platform training dataset. This study developed a planetary-scale multimodal dataset to train MarScope. Although MarScope is designed for Martian surface analysis, its training data are not limited to Mars. To preserve cross-planet extensibility, this study constructed a planetary-scale multimodal dataset comprising more than 200,000 image-text pairs that capture geomorphological features from Mars, the Moon, Mercury, and several icy satellites. Images were collected from high-resolution orbital datasets including HiRISE website, peer-reviewed literature and official NASA and ESA releases.

Besides, a large language model (LLM)-assisted curation workflow was employed to address the redundant and inconsistent information in the original texts. The LLM performed relevance filtering, key-phrase extraction, and semantic rewriting to refine each caption (48). Additional data augmentation (48), through synonym expansion and paraphrasing, was used to enhance linguistic diversity and reduce overfitting to specific wording. The resulting dataset spans a broad range of geomorphological classes, imaging geometries, and illumination conditions, enabling the model to generalize across planetary environments and spatial scales.

Vision-language platform semantic encoding and feature alignment. MarScope was trained with a contrastive learning objective that aligns visual and textual embeddings within a shared semantic space (49). The network maximizes similarity between matched image–text pairs and minimizes it between mismatched pairs. Each planetary image patch is then represented as a high-dimensional embedding vector.

A zero-shot classification setup was used to identify the optimal model checkpoint (11). In this setting, the pretrained encoder was applied directly without additional fine-tuning, and image embeddings were compared against textual prompts representing geomorphological classes (e.g., “crater,” “yardang,” “transverse aeolian ridge”) from benchmark Mars datasets such as DoMars16k (50) and the HiRISE v3 dataset (51). Measures of classification accuracy and the semantic alignment between visual and textual representations were used solely to determine the checkpoint with the most reliable parameter configuration for deployment.

Platform implementation: hierarchical search framework and near-instantaneous query system. To enable large-scale semantic retrieval and analysis, all image embeddings produced by the trained model were indexed within a Facebook AI Similarity Search (FAISS)-based approximate nearest-neighbor (ANN) database (52). The global Mars CTX mosaic (9; 13) was divided into overlapping tiles (~130 Million) at two hierarchical resolutions (0.2° and 0.02°) to balance global coverage with local detail. Each tile’s visual embedding, produced by the trained encoder, was stored as a high-dimensional vector linked to geospatial metadata. This approach effectively reduced the raw imagery by approximately 160×, from 900 GB to 5.7 GB at 0.2° resolution and 2.2 TB to 14 GB at 0.02° , while preserving key semantic information.

Cross-modal retrieval was implemented within the shared embedding space, where similarity between image and text embeddings is measured using cosine distance. Text queries were first encoded using the trained text encoder, and the resulting vectors were used to retrieve the most similar image embeddings (53). This procedure underpins all retrieval modes (53), including image, text, and image-text multimodal searches.

To examine retrieval consistency and refine the similarity threshold, the top ten matches and ten near-threshold samples were visually inspected. The near-threshold cases were used to adjust the decision boundary and ensure stable retrieval behavior across heterogeneous landform types.

For visualization and subsequent geospatial analysis, retrieved embeddings were mapped back to their original planetary coordinates to generate spatial distribution map and density map. In addition, all retrieval results, including coordinates information and image clips, can be exported for downstream analyses.

Evaluation with published catalogue. To quantitatively evaluate the retrieval performance of MarScope, we compare our retrieval results with previously published global catalogues (14–19). Six types were selected for validation: alluvial fans (14), glacier-like forms (15), landslides (16), pitted cones (17), yardangs (18) and dark slope streak (19). For each landform type, the published catalogue provides a set of reference points $G = \{g_1, g_2, \dots, g_M\}$, which is expressed as planetocentric latitude and longitude. Since every image patch in our MarScope database is georeferenced, we transfer the top- K retrieved image patches to a set of center coordinates $P = \{p_1, p_2, \dots, p_M\}$. Consequently, we formulate our evaluation as a point-set matching problem between the predicted locations and the ground truth catalog.

Given the continuous nature of geospatial coordinates, it is infeasible to exact positional coincidence. Instead, we develop a proximity-based matching criterion with a tolerance radius r (set to 0.5° in this study) during matching. In other words, we regard a retrieved patch as correctly matched if the nearest-neighbor distance to the corresponding ground-truth point is below the threshold. According to the above criterion, we define the following three metrics:

$$Precision@K = \frac{1}{K} \sum_{i=1}^K \mathbb{I} \left(\min_{g \in G} \| p_i - g \| \leq r \right) \quad (1)$$

$$Recall@K = \frac{1}{M} \sum_{j=1}^M \mathbb{I} \left(\min_{p \in P_K} \| p - g_j \| \leq r \right) \quad (2)$$

$$F1@K = 2 \cdot \frac{Precision@K \cdot Recall@K}{Precision@K + Recall@K} \quad (3)$$

where $\mathbb{I}(\cdot)$ denotes the indicator function. Here, precision serves as a measure of retrieval fidelity, which indicates the percentage of candidates spatially validated by the catalogue. Conversely, Recall quantifies the completeness of the global mapping, representing the fraction of catalogue entries that are successfully recovered by MarScope. Since increasing the retrieval depth

K inherently presents a trade-off between Recall and Precision, we utilize the $F1@K$ to identify the optimal sensitivity.

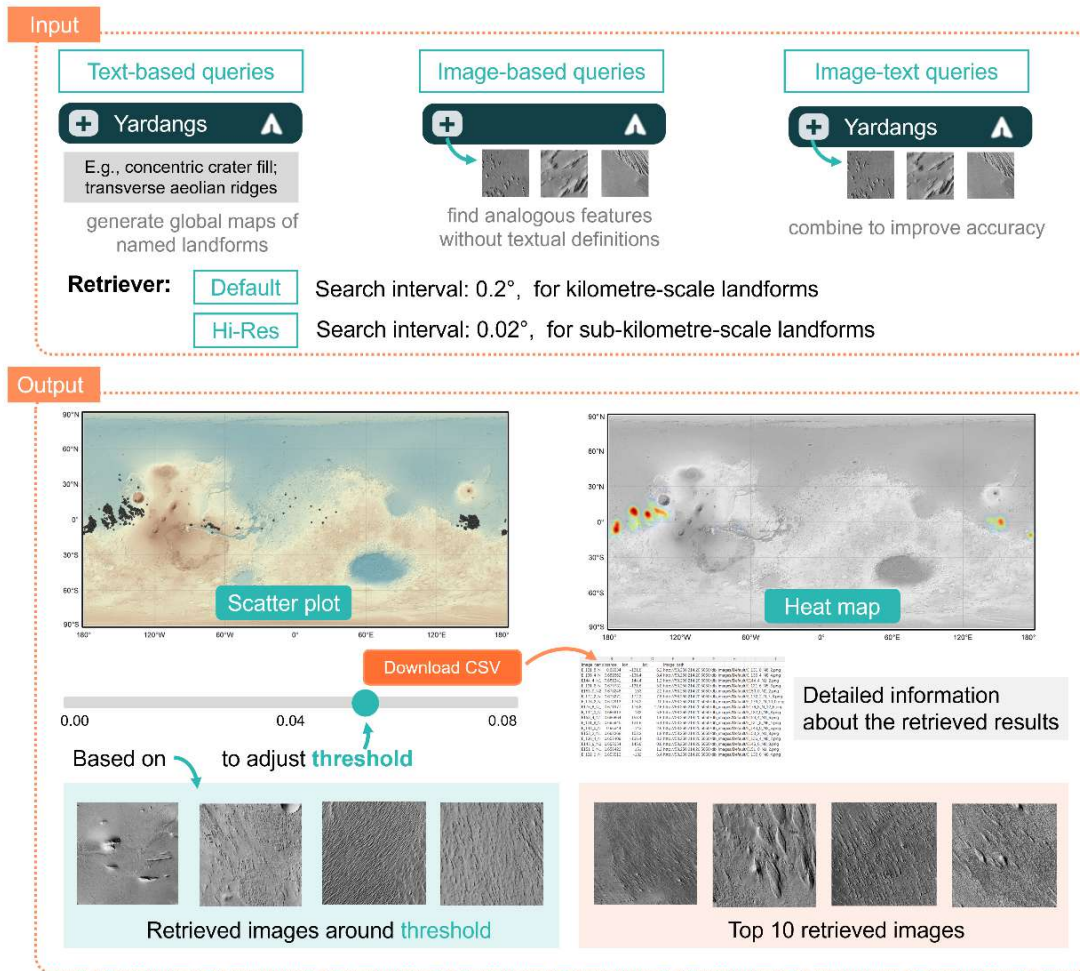


Figure 1: Workflow of the MarScope platform. MarScope enables three query modes—text-based, image-based, and image-text—to retrieve Martian landforms. The system outputs global distribution maps, heat maps, detailed records, and curated image sets, supporting both mapping and dataset construction.

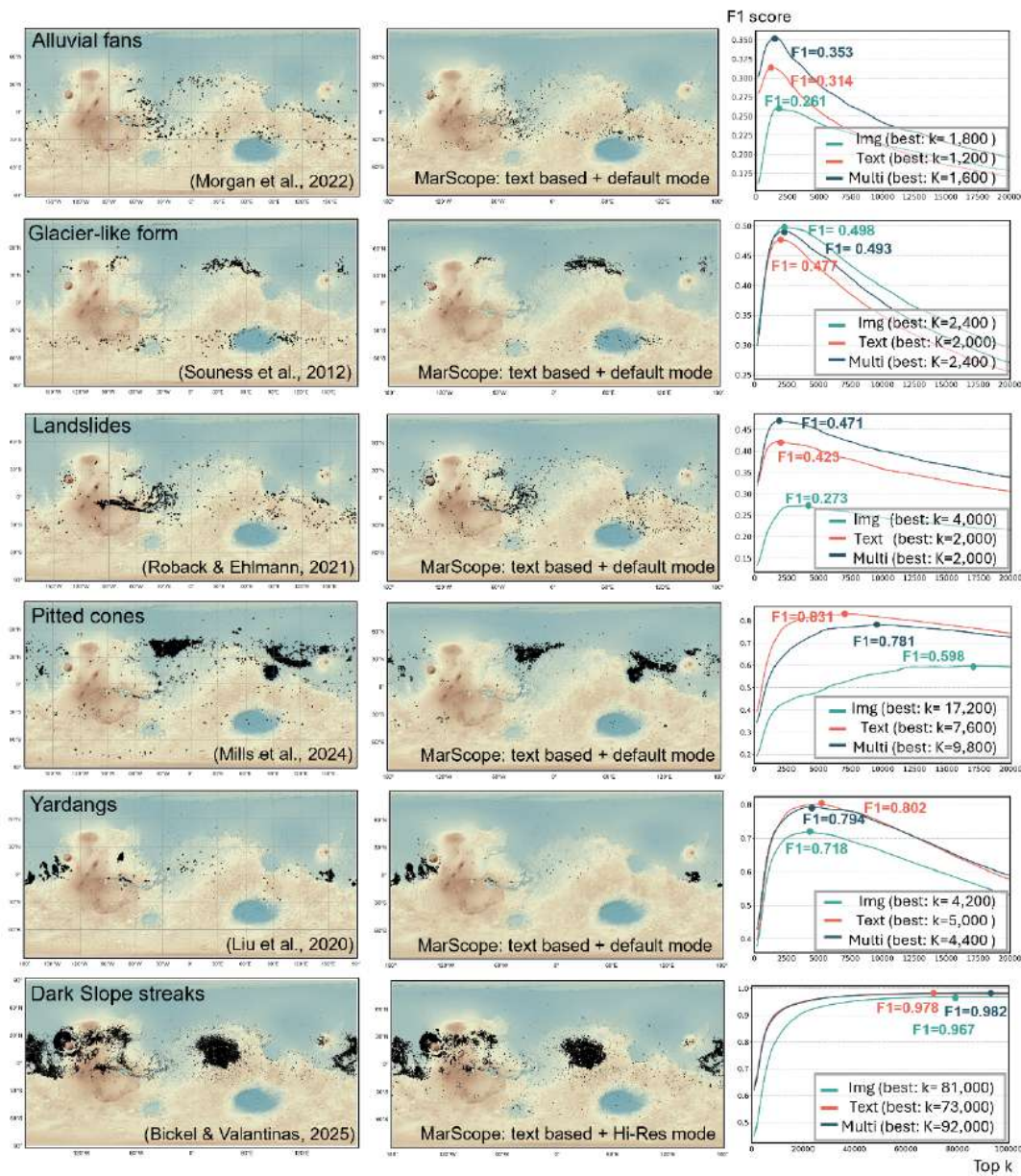


Figure 2: Validation of MarScope outputs. Left column: Published global distributions for six representative Martian landforms: alluvial fans (14), glacier-like forms (15), landslides (16), pitted cones (17), yardangs (18), and dark slope streaks (19). Middle column: corresponding MarScope retrievals generated using text-mode queries, with the Hi-Res mode applied to dark slope streaks and the default mode used for the other five landforms. Right column: dynamic F1 scores as a function of the top-K retrieved tiles for image (green), text (red), and multi-modal (blue) query modes. Peak F1 values and the corresponding K are shown for each landform type.

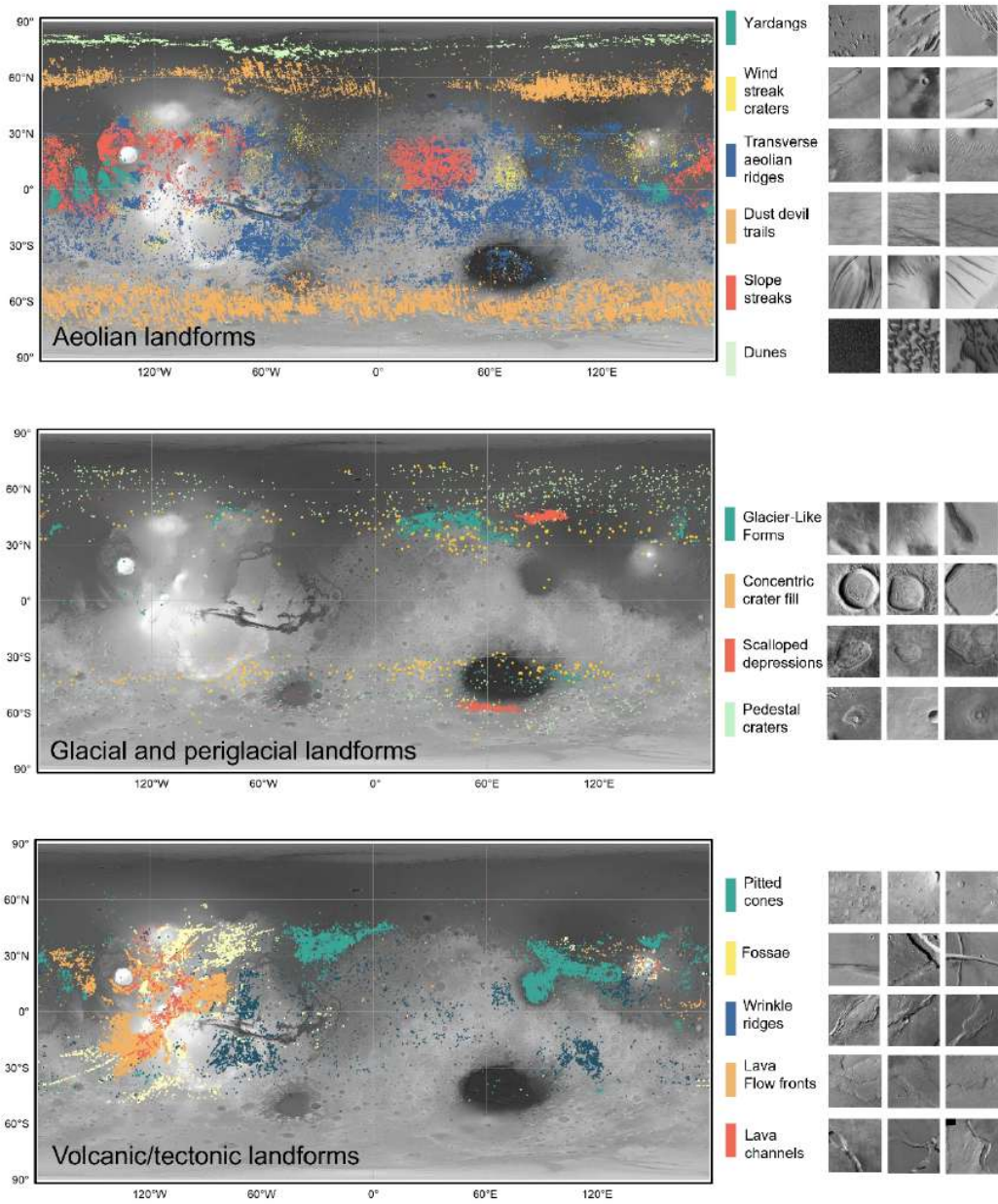


Figure 3: Landform distributions retrieved by MarScope. Global maps of aeolian (top), glacial and periglacial (middle), and volcanic/tectonic (bottom) landforms on Mars. Colors indicate landform classes, with representative CTX patches on the right showing characteristic morphologies.

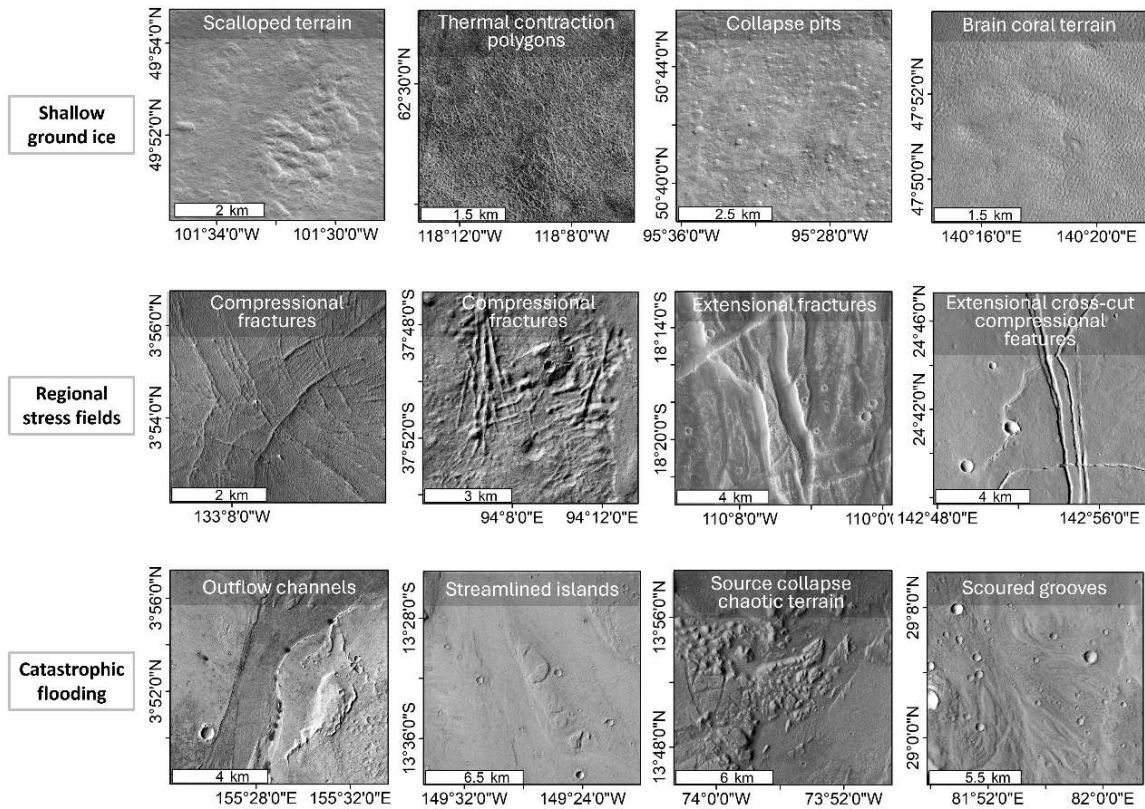


Figure 4: Process-based geomorphological mapping enabled by MarScope. Examples retrieved using formation-mechanism-oriented queries, including shallow ground ice, regional stress fields, and catastrophic flooding.

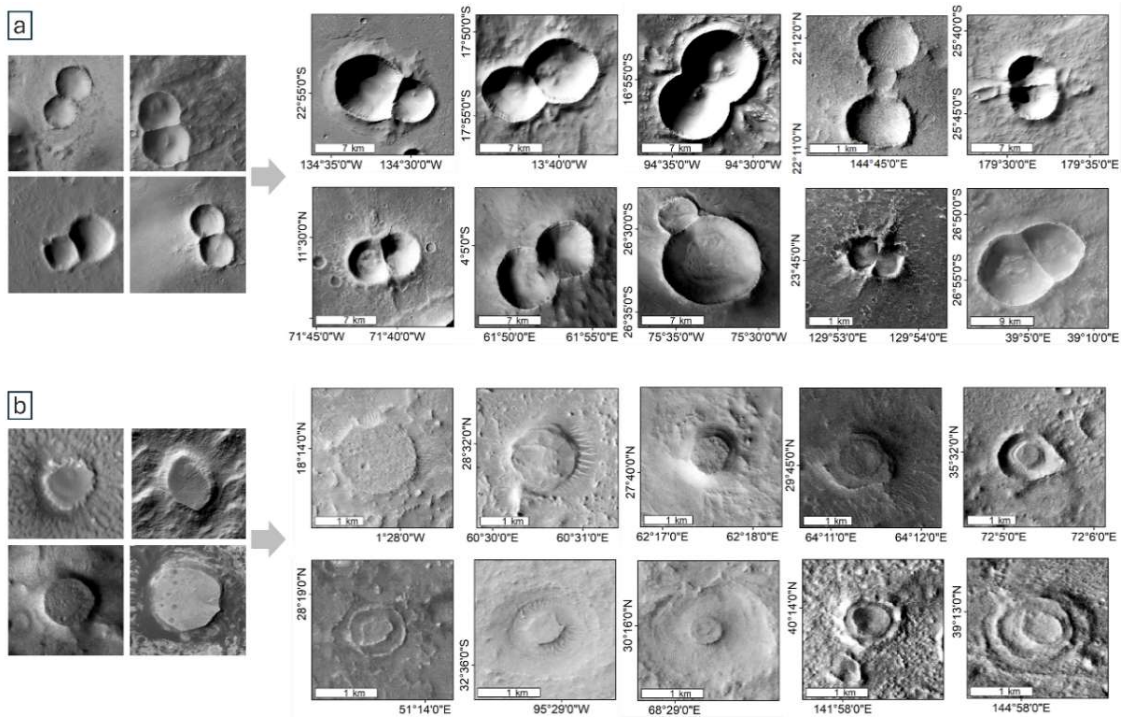


Figure 5: Visual discovery of rare Martian landforms using MarScope. Retrieval of (A) doublet craters and (B) inverted craters, showing reference examples (left) and morphologically similar features identified across global CTX data (right).

Acknowledgments

We thank the mission teams of NASA for providing open-access planetary datasets used in this study, including HiRISE, CTX and other publicly available archives. Language polishing and refinement of the manuscript were assisted by ChatGPT (version 5.2), and the authors take full responsibility for the content.

Funding: This work was funded by the National Natural Science Foundation of China (42578017, 42272274, 42273041) and Key Technology Research Project of TW-3 (TW3004).

Competing interests: The authors declare no competing interests.

Data and materials availability: The MarScope can be researched at <http://marscope.site/>. Remote sensing datasets (CTX imagery) are publicly available at <https://murray-lab.caltech.edu/CTX/>.

References and Notes

- [1] R. Sullivan et al. Aeolian processes at the Mars Exploration Rover Meridiani Planum landing site. *Nature*, 436:58–61, 2005.
- [2] J. Liu et al. Martian dunes indicative of wind regime shift in line with end of ice age. *Nature*, 620:303–309, 2023.
- [3] Stephanie C. Werner. The global martian volcanic evolutionary history. *Icarus*, 201(1):44–68, 2009.
- [4] Stuart J. Robbins, Gaetano Di Achille, and Brian M. Hynek. The volcanic history of Mars: High-resolution crater-based studies of the calderas of 20 volcanoes. *Icarus*, 211(2):1179–1203, 2011.
- [5] Victor R. Baker. Geomorphological evidence for water on Mars. *Elements*, 2(3):139–143, 2006.

- [6] Caleb I. Fassett and James W. Head III. The timing of martian valley network activity: Constraints from buffered crater counting. *Icarus*, 195(1):61–89, 2008.
- [7] F. Forget, R. M. Haberle, F. Montmessin, B. Levrard, and J. W. Head. Formation of glaciers on Mars by atmospheric precipitation at high obliquity. *Science*, 311:368–371, 2006.
- [8] J. W. Head III et al. Global distribution of large lunar craters: Implications for resurfacing and impactor populations. *Science*, 329:1504–1507, 2010.
- [9] M. C. Malin et al. Context Camera Investigation on board the Mars Reconnaissance Orbiter. *J. Geophys. Res. Planets*, 112:2006JE002808, 2007.
- [10] A. S. McEwen et al. Mars Reconnaissance Orbiter’s High Resolution Imaging Science Experiment (HiRISE). *J. Geophys. Res. Planets*, 112, 2007.
- [11] Alec Radford, Jong Wook Kim, Chris Hallacy, Aditya Ramesh, Gabriel Goh, Sandhini Agarwal, Girish Sastry, Amanda Askell, Pamela Mishkin, Jack Clark, et al. Learning transferable visual models from natural language supervision. In *International conference on machine learning*, pages 8748–8763. PMLR, 2021.
- [12] J. L. Dickson, L. A. Kerber, C. I. Fassett, and B. L. Ehlmann. A global, blended CTX mosaic of Mars with vectorized seam mapping: A new mosaicking pipeline using principles of non-destructive image editing, 2018. LPSC, 2480.
- [13] J. L. Dickson, B. L. Ehlmann, L. H. Kerber, and C. I. Fassett. Release of the global CTX mosaic of Mars: An experiment in information-preserving image data processing. *LPSC*, 2806:2353, 2023.
- [14] A. M. Morgan, S. A. Wilson, and A. D. Howard. The global distribution and morphologic characteristics of fan-shaped sedimentary landforms on Mars. *Icarus*, 385:115137, 2022.
- [15] C. Souness, B. Hubbard, R. E. Milliken, and D. Quincey. An inventory and population-scale analysis of martian glacier-like forms. *Icarus*, 217:243–255, 2012.
- [16] K. P. Roback and B. L. Ehlmann. Controls on the global distribution of martian landslides. *J. Geophys. Res. Planets*, 126:e2020JE006675, 2021.

- [17] M. M. Mills, V. T. Bickel, A. S. McEwen, and A. Valantinas. A global dataset of pitted cones on Mars. *Icarus*, 418:116145, 2024.
- [18] J. Liu et al. Mapping and spatial statistical analysis of Mars Yardangs. *Planet. Space Sci.*, 192:105035, 2020.
- [19] V. T. Bickel and A. Valantinas. Streaks on martian slopes are dry. *Nat. Commun.*, 16:4315, 2025.
- [20] G. Portyankina, A. Pommerol, K.-M. Aye, C. J. Hansen, and N. Thomas. Observations of the northern seasonal polar cap on Mars II: HiRISE photometric analysis of evolution of northern polar dunes in spring. *Icarus*, 225:898–910, 2013.
- [21] C. J. Hansen et al. Seasonal erosion and restoration of Mars’ northern polar dunes. *Science*, 331:575–578, 2011.
- [22] I. J. Daubar et al. Global distribution of dust devil tracks on Mars. *Geophys. Res. Lett.*, 52:e2024GL114393, 2025.
- [23] D. C. Berman, M. R. Balme, S. C. R. Rafkin, and J. R. Zimbelman. Transverse aeolian ridges (TARs) on Mars II: Distributions, orientations, and ages. *Icarus*, 213:116–130, 2011.
- [24] D. Reiss, S. van Gasselt, G. Neukum, and R. Jaumann. Absolute dune ages and implications for the time of formation of gullies in Nirgal Vallis, Mars. *J. Geophys. Res. Planets*, 109, 2004.
- [25] S. Gou et al. Transverse aeolian ridges in the landing area of the Tianwen-1 Zhurong rover on Utopia Planitia, Mars. *Earth Planet. Sci. Lett.*, 595:117764, 2022.
- [26] Y. Lu et al. Aeolian disruption and reworking of TARs at the Zhurong rover field site, southern Utopia Planitia, Mars. *Earth Planet. Sci. Lett.*, 595:117785, 2022.
- [27] D. C. Berman, M. R. Balme, J. R. Michalski, S. C. Clark, and E. C. Joseph. High-resolution investigations of transverse aeolian ridges on Mars. *Icarus*, 312:247–266, 2018.

- [28] L. Kerber and J. W. Head. A progression of induration in Medusae Fossae Formation transverse aeolian ridges: evidence for ancient aeolian bedforms and extensive reworking. *Earth Surf. Process. Landf.*, 37:422–433, 2012.
- [29] V. T. Bickel. Dust, sand and wind drive slope streaks on Mars. *Nat. Commun.*, 16:9583, 2025.
- [30] J. Veverka, P. Gierasch, and P. Thomas. Wind streaks on Mars: Meteorological control of occurrence and mode of formation. *Icarus*, 45:154–166, 1981.
- [31] S. J. Kadish, N. G. Barlow, and J. W. Head. Latitude dependence of Martian pedestal craters: Evidence for a sublimation-driven formation mechanism. *J. Geophys. Res. Planets*, 114, 2009.
- [32] S. J. Kadish, J. W. Head, and N. G. Barlow. Pedestal crater heights on Mars: A proxy for the thicknesses of past, ice-rich, amazonian deposits. *Icarus*, 210:92–101, 2010.
- [33] B. Hubbard, C. Souness, and S. Brough. Glacier-like forms on Mars. *The Cryosphere*, 8:2047–2061, 2014.
- [34] J. Levy, J. W. Head, and D. R. Marchant. Concentric crater fill in the northern mid-latitudes of Mars: Formation processes and relationships to similar landforms of glacial origin. *Icarus*, 209:390–404, 2010.
- [35] T. W. Haltigin, W. H. Pollard, P. Dutilleul, G. R. Osinski, and L. Koponen. Co-evolution of polygonal and scalloped terrains, southwestern Utopia Planitia, Mars. *Earth Planet. Sci. Lett.*, 387:44–54, 2014.
- [36] A. Séjourné et al. Scalloped depressions and small-sized polygons in western Utopia Planitia, Mars: A new formation hypothesis. *Planet. Space Sci.*, 59:412–422, 2011.
- [37] J. B. Plescia. Graben and extension in northern Tharsis, Mars. *J. Geophys. Res. Planets*, 96:18883–18895, 1991.
- [38] F. Borraccini, L. Lanci, F. C. Wezel, and D. Baioni. Crustal extension in the Ceraunius Fossae, northern Tharsis region, Mars. *J. Geophys. Res. Planets*, 110, 2005.

- [39] E. Theilig and R. Greeley. Lava flows on Mars: Analysis of small surface features and comparisons with terrestrial analogs. *J. Geophys. Res. Solid Earth*, 91:E193–E206, 1986.
- [40] J. E. Bleacher et al. Olympus Mons, Mars: Inferred changes in late amazonian aged effusive activity from lava flow mapping of Mars Express High Resolution Stereo Camera data. *J. Geophys. Res. Planets*, 112, 2007.
- [41] D. A. Williams, R. Greeley, E. Hauber, K. Gwinner, and G. Neukum. Erosion by flowing Martian lava: New insights for Hecates Tholus from Mars Express and MER data. *J. Geophys. Res. Planets*, 110, 2005.
- [42] T. Ruj and K. Kawai. A global investigation of wrinkle ridge formation events; implications towards the thermal evolution of Mars. *Icarus*, 369:114625, 2021.
- [43] Z. Chen et al. A global database of pitted cones on Mars for research on Martian volcanism. *Sci. Data*, 11:942, 2024.
- [44] L. Wang, J. Zhao, J. Huang, and L. Xiao. An explosive mud volcano origin for the pitted cones in southern Utopia Planitia, Mars. *Sci. China Earth Sci.*, 66:2045–2056, 2023.
- [45] E. M. McGowan. The Utopia/Isidis overlap: Possible conduit for mud volcanism on Mars. *Icarus*, 212:622–628, 2011.
- [46] D. E. Vavilov et al. Evidence for widely-separated binary asteroids recorded by craters on Mars. *Icarus*, 383:115045, 2022.
- [47] C. F. Pain, J. D. A. Clarke, and M. Thomas. Inversion of relief on Mars. *Icarus*, 190:478–491, 2007.
- [48] M. U. Khattak, S. Kunhimon, M. Naseer, S. Khan, and F. S. Khan. Unimed-clip: Towards a unified image-text pretraining paradigm for diverse medical imaging modalities, 2024. ArXiv Prepr. ArXiv241210372.
- [49] A. Radford et al. Learning transferable visual models from natural language supervision. *Preprint at <http://arxiv.org/abs/2103.00020>*, 2021.

- [50] T. Wilhelm et al. DoMars16k: A diverse dataset for weakly supervised geomorphologic analysis on Mars. *Remote Sens.*, 12:3981, 2020.
- [51] K. Wagstaff et al. Mars image content classification: Three years of NASA deployment and recent advances. In *Proceedings of the AAAI Conference on Artificial Intelligence*, volume 35, pages 15204–15213, 2021.
- [52] M. Douze et al. The faiss library. *IEEE Trans. Big Data*, pages 1–17, 2025.
- [53] G. Gu, S. Chun, W. Kim, Y. Kang, and S. Yun. Language-only training of zero-shot composed image retrieval. In *Proceedings of the IEEE/CVF Conference on Computer Vision and Pattern Recognition*, pages 13225–13234, 2024.